

Procedural and learning-based generation of coral reef islands

Submission1265



Figure 1: From top-view and profile-view sketches, our system procedurally generates coral reef islands and trains a cGAN to produce diverse and realistic terrains.

Abstract

We propose a procedural method for generating single volcanic islands with coral reefs using user sketching from two projections: a top view, which defines the island's shape, and a profile view, which outlines its elevation. These projections, commonly used in geological and remote sensing domains, are complemented by a user-defined wind field, applied as a distortion field to deform the island's shape, mimicking the effects of wind and waves on the long term and enabling finer user control. We then model the growth of coral on the island and its surrounding to construct the reef following biological observations. Based on these inputs, our method generates a height field of the island. Our method is capable of creating a large variety of island models composing a dataset used for training a conditional Generative Adversarial Network (cGAN). By applying data augmentation, the cGAN allows for even greater variety in the generated islands, providing users with higher freedom and intuitive controls over the shape and structure of the final output.

1 **Keywords:** Procedural modeling, Terrain generation, cGAN,
2 Coral reef, Sketch-based interface

3 1. Introduction

4 Simulating the formation of coral reef islands presents significant
5 challenges due to the complex interplay of geological, environmental-
6 and biological factors (Hopley, 2014). One major difficulty lies
7 in capturing the long-term subsidence of volcanic islands, which
8 occurs over millions of years, while simultaneously modeling the
9 upward growth of coral reefs that rely on environmental conditions
10 such as water depth, temperature, and sunlight. This combination of
11 slow geological processes and dynamic biological growth is chal-
12 lenging to replicate in a computational model.

13 Additionally, the biological aspects of coral growth are inher-
14 ently tied to environmental factors. Coral reefs grow only within a
15 specific range of water depth and sunlight, and their growth patterns
16 are affected by the health of the reef ecosystem and the availability
17 of resources. Accurately modeling these biological dependencies in
18 a procedural system is challenging, as these factors are numerous

19 and difficult to generalize. Moreover, the scarcity of data available
20 obstructs the global understanding of these ecosystems. In a recent
21 high-resolution mapping of shallow coral reefs (Lyons et al., 2024),
22 researchers estimated the total surface area of this biome to cover
23 less than 0.7% of Earth's area, and more specifically that coral habi-
24 tation represents less than 0.2%.

25 Moreover, the need to design plausible reef structures in digi-
26 tal environments for applications such as scientific visualization,
27 simulation, or digital entertainment, calls for models that balance
28 realism with controllability. Existing terrain generation methods,
29 such as Perlin noise-based algorithms or uplift-erosion models, are
30 often ill-suited for these processes. While they can generate natural-
31 looking landscapes (such as alpine landscape, representing about a
32 quarter of land area (Körner et al., 2014)), they do not account for
33 the unique geological and biological interactions that govern coral
34 reef island formation, thus missing coherency. Capturing these dy-
35 namics, while also providing user control during the modeling of a
36 terrain, requires a balance between realism and flexibility, allowing
37 for both accurate computationally expensive simulation of natural
38 processes and intuitive user control in interactive time.

Despite advances in terrain generation, existing methods struggle with user-controlled design of specific island shapes and achieving realism without real data. Coral reef islands exemplify this gap: we lack datasets to directly train deep models, and purely procedural methods require expert tuning to mimic their features.

To address these issues, we propose to use curve-based modeling techniques as an initial step in our approach as a means to efficiently create a large and diverse set of training examples for a learning-based model. Each synthetic example is represented by a terrain height field and a corresponding semantic label map that marks different regions, providing structured input-output pairs for the learning stage.

We trained a conditional Generative Adversarial Network (cGAN) as the core of our learning-based approach (Mirza and Osindero, 2014; Isola et al., 2017). A cGAN is a type of deep learning model that learns to generate realistic data based on an input condition or context. In our case, the cGAN takes as input the semantic label map of an island generated by the procedural step and learns to produce a realistic island height field that matches this layout. By training on a large variety of examples from our curve-based algorithm, the cGAN captures the subtle terrain features and variations characteristic of coral reef islands, this approach surpasses the capabilities of traditional procedural rules, aided by extensive data augmentation. The cGAN model can be used on its own to generate new island terrains with simplified and more intuitive user inputs through digital drawing, and the model will generate a realistic island terrain accordingly.

The key contributions are as follows: 1) a novel curve-based procedural algorithm for shaping island terrains from top and profile views, 2) The training of a deep learning model on synthetic data derived from procedural rules, serving as an abstraction layer that hides underlying complexity, 3) A demonstration that the cGAN approach tolerates imprecise, low-detail user input sketches, broadening usability, without the need for cutting-edge network architectures, and 4) An insight that procedural generation remains essential to produce training data in data-sparse domains such as coral reef islands. These contributions collectively show a pathway to blend user-driven design with learning-based generation in terrain modeling.

2. Related work

Procedural terrain generation spans a spectrum from purely noise-driven algorithms to physics-based simulations and, more recently, data-driven methods. In the context of coral reef islands, where both long-term geological subsidence and biogenic reef accretion interplay, existing approaches fall short in one of two ways: either they lack ecological or geological grounding, or they offer insufficient authoring control.

Procedural and simulation-based methods Noise-based techniques such as Perlin noise (Perlin, 1985), Simplex noise (Perlin, 2001), and the Diamond-Square algorithm (Fournier et al., 1982) (often extended via fBm or multifractal noise (Musgrave et al., 1989; Ebert et al., 2003)) remain popular for their simplicity and speed. Island shapes are generated by modulating noise with radial falloff masks (Olsen, 2004), but these methods cannot reproduce

reef rings, lagoons, or atoll structures in a geologically coherent manner. They treat terrain purely as a signal-processing problem, separated from processes like volcanic subsidence or coral growth (Smelik et al., 2009; Galin et al., 2019).

Simulation-based approaches introduce surface deformations by modeling erosion (Beneš et al., 2006; Neidhold et al., 2005; Mei et al., 2007), tectonic uplift (Cordonnier, Braun, et al., 2016; Cordonnier, Cani, et al., 2017; Schott et al., 2023), or vegetation-terrain feedback (Ecormier-Nocca et al., 2021; Cordonnier, Galin, et al., 2017). Hydraulic and thermal erosion capture fluvial networks and slope-driven mass wasting, but they omit underwater sedimentation and biogenic carbonate accretion. Tectonic and isostatic models excel at orogeny but ignore coral reef dynamics, while vegetation-based methods do not generalize to marine ecosystems. Consequently, none of these simulations jointly capture the slow subsidence of volcanic islands and the compensatory growth of surrounding reefs on the timescales required for atoll formation.

Sketch-based terrain modeling Sketch-driven interfaces bridge user intent and procedural detail. Curve-based systems let users draw ridges, valleys, or coastlines that guide surface deformation and noise propagation (Gain et al., 2009; Hnaiid et al., 2010). Constraint-based methods extend this by enforcing absolute elevation or slope values at control curves or points, solved via diffusion or fractal interpolation (Gasch et al., 2020; Talgorn and Belhadj, 2018), and even gradient-domain editing for slope control (Guérin, Peytavie, et al., 2022). Semantic approaches encode high-level "terrain atoms" from a dictionary of primitives (Génevaux et al., 2015) or interpret geological schematics into 3D models (Natali et al., 2012). While these techniques grant artists fine-grained control, they typically lack ecological constraints and have not been tailored to marine biogeomorphology.

Learning-based terrain synthesis Deep generative models offer a way to learn complex patterns without explicit procedural rules. Unconditional GANs have been applied to digital elevation maps of mountains (Wulff-Jensen et al., 2018) and joint height-texture synthesis (Spick and Walker, 2019), but their reliance on latent noise prevents precise layout control. Two-stage pipelines use an initial GAN for heightmaps and a conditional GAN for textures (Beckham and Pal, 2017) or reverse the order (imagery-to-DEM) (Panagiotou and Charou, 2020), yet still lack the ability to guide authoring.

Conditional GANs (cGANs) extend image-to-image translation methods such as pix2pix (Isola et al., 2017) to terrain, enabling sketch- or label-map-conditioned generation. Prior work includes sketch-to-DEM translation for generic landforms (Guérin, Digne, Galin, Peytavie, et al., 2017) and sparse "altitude dot" conditioning (Voulgaris et al., 2021), as well as cGANs that invert satellite imagery into elevation (Sisodia, 2022). However, these models require extensive paired real-world datasets which are scarce for coral reef islands.

3. Overview

Our method for procedural generation of coral reef islands is composed of two independent modeling techniques shown in Figure 2. A first curve-based algorithm (top-left blue block, presented in Section 4), parametrize the surface of islands by a top-view sketch in-

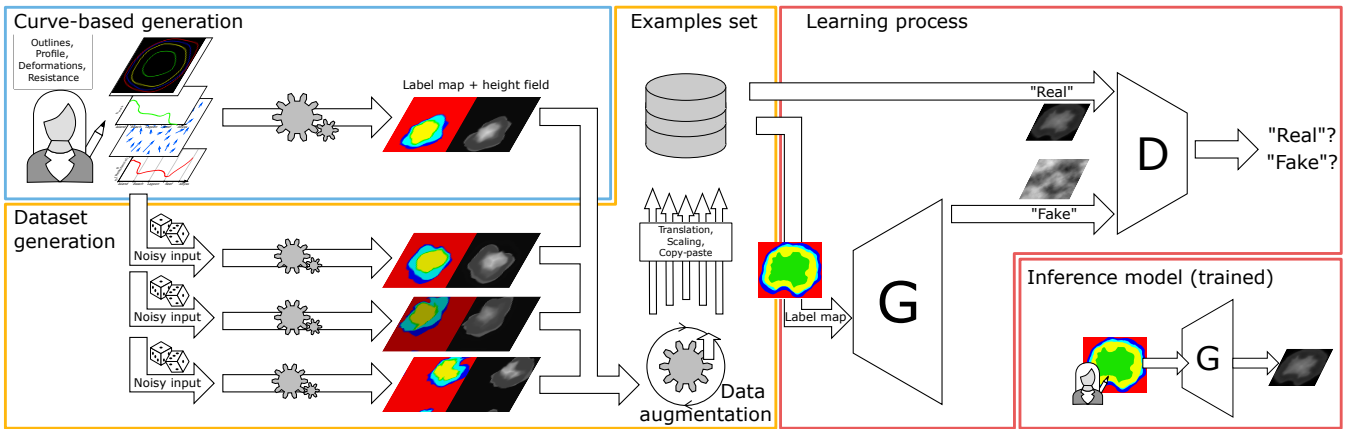


Figure 2: Our pipeline first prompt our user to create single pairs of coral reef islands' height fields and label maps using our proposed curve-based modeling algorithm (Section 4). The same algorithm is applied multiple times on randomly altered versions of the user input to create a dataset, which we further enhance with data augmentation techniques Section 5. Finally, we train a conditional Generative Adversarial Network which can then be used standalone to create height fields from labeled sketches (Section 6).

147 interface, describing the outlines of the regions composing it and a
 148 stroke-based wind field deforming them, as well as a profile-view
 149 sketch describing for each region its altitude and resistance to de-
 150 formations. User inputs are given as 1D functions (altitude and re-
 151 sistance), a 1D polar function (island outlines) and a 2D vector field
 152 (wind field) as shown in Figure 3, which are convient to randomize
 153 through the use of noise, but hindering users' modeling freedom.

154 We propose a second learning-based generation algorithm (right
 155 red blocks Figure 2, developed in Section 6), which trains a neural
 156 generator G to transform a labeled image into a height field. Paral-
 157 lelly, a discriminator D is train to distinguish height fields provided
 158 from the training set against height fields generated by G . This ad-
 159 versarial training strengthen the outputs of the generator, up to the
 160 point where we discard the discriminator and training data, only
 161 keeping the generation step (bottom-right). Users are then able to
 162 provide unseen label maps and obtain height fields as close as pos-
 163 sible to the training dataset. This method for terrain modeling is
 164 poorly constraint, however requires a large amount of prior data in
 165 its training set, which are not available in our case.

166 We connect these two algorithms through a process of dataset
 167 generation (central orange block Figure 2, described in Section 5)
 168 in order to enforce the benefits of each while reducing their limita-
 169 tions. Given the initial curve-based user inputs, we create a dataset
 170 composed of similar samples processed by our first algorithm, ras-
 171 terized into a 2D image of the parametrized regions, and paired
 172 with the resulting height field. We then enhance greatly the size
 173 of the dataset by employing various data augmentation techniques
 174 such as translations, scaling and copy-pasting of multiple islands in
 175 a single sample. We then obtain a dataset large enough for training
 176 our cGAN and enable the modeler to create procedurally coral reef
 177 islands with a high level of control.

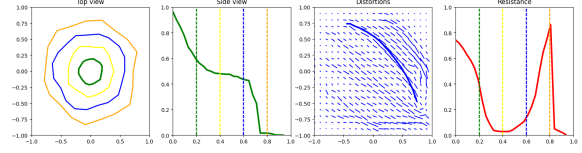


Figure 3: The user can interact directly on the island by editing the different canvases in no specific order. This UI shows, from left to right, the top-view sketch with the different outlines of each regions, the profile-view sketch with the outlines represented in dotted lines, the wind velocity sketch drawn with strokes (last stroke is visible), and the resistance function showing here a high resistance at the top of the island and on the front reef.

178 4. Curve-based island generation

179 The generation of coral reef island terrains involves a structured
 180 process that takes the user's sketches and produces a complete 3D
 181 terrain model. This process begins with the creation of the initial
 182 height field based on the user's input, followed by the application
 183 of wind deformation to introduce natural variations, and concludes
 184 with the integration of coral reef features through subsidence and
 185 coral growth modeling.

186 The generation of coral reef islands in our system begins with
 187 two intuitive curve-based inputs from the user: a top-view sketch
 188 and a profile-view sketch, which define the islands horizontal lay-
 189 out and vertical elevation profile. In addition to these sketches, the
 190 user can further refine the terrain by applying wind deformation
 191 strokes, which simulate the effects of wind and waves on the is-
 192 lands shape. This combination of sketches and wind inputs gives
 193 users precise control over both the islands structure and its natural
 194 variations, such as irregular coastlines or concave features. We will
 195 present the usefulness of these sketches in this section, and describe
 196 the technical details in the next section.

197 4.1. Initial height field generation

198 The top-view sketch defines the island's outline as seen from above.
 199 Using a simple drawing interface, the user delineates concentric
 200 boundaries for key regions such as the island itself, the beaches, the
 201 lagoon, and the surrounding abyss, around the canvas center. Each
 202 boundary is represented in polar coordinates, where r_p is the radial
 203 distance from the island's center and θ_p is the angular position.
 204 Allowing r to vary with θ introduces irregular, natural shapes rather
 205 than perfect circles (Figure 4).

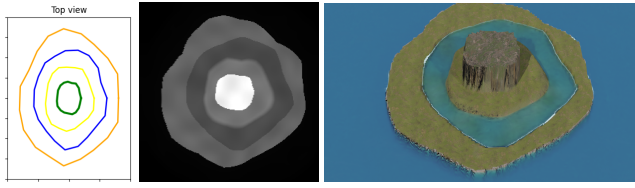


Figure 4: Using only the outlines from the top-view sketch, each point in the field is assigned a region (island, beach, lagoon, abyss), which later guides its height assignment.

206 The profile-view sketch defines the island's vertical elevation
 207 along any radial direction. Here, the user draws a curve that specifies
 208 height at key terrain milestones, such as the central peak, island
 209 border, beach, lagoon, and abyss, creating a continuous 1D height
 210 function $h_{\text{profile}}(\tilde{x})$ where \tilde{x} is a parametric distance measuring position
 211 along the sequence of regions. This continuous profile ensures
 212 smooth elevation transitions across all terrain features.

213 By combining the top-view and profile-view sketches via revolution modeling,
 214 the system generates a full 3D terrain model that matches the user's design. The process begins
 215 by transforming those two sketches into a coherent height field (Figure 6).

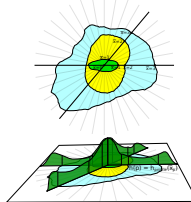


Figure 5: Parametric distance \tilde{x} depending on angle θ .

219 For any point \mathbf{p} on the terrain, the system
 220 computes polar coordinates (r_p, θ_p) . The radial distance r_p determines which region
 221 the point belongs to (island, beach, lagoon,
 222 reef, or abyss) based on the user-defined ra-
 223 dial limits. Those outlines from the top-view
 224 sketch provide the exact boundaries between
 225 regions.

227 Each point's height is computed using the
 228 profile function $h_{\text{profile}}(\tilde{x})$. Instead of using
 229 the raw radial distance r_p , we define a parametric region distance \tilde{x}_p
 230 that maps each point to a normalized position along the concentric
 231 regions (see Figure 5). The radial space is divided by user-defined
 232 boundaries R_0, R_1, \dots, R_n , corresponding to the island center, border,
 233 beach, lagoon, and abyss.

234 When a point \mathbf{p} lies between two boundaries, say R_i and R_{i+1} ,
 235 its parametric distance is

$$\tilde{x}_{\mathbf{p}} = i + \frac{r_{\mathbf{p}} - R_i}{R_{i+1} - R_i}, \quad (1)$$

236 where i is the index of the region containing \mathbf{p} (i.e., $R_i \leq r_{\mathbf{p}} <$

R_{i+1}). This linear mapping stretches each region's radial span to the interval $[i, i+1]$, ensuring smooth interpolation across region boundaries. The final height at point \mathbf{p} is then $h(\mathbf{p}) = h_{\text{profile}}(\tilde{x}_{\mathbf{p}})$.

240 4.1.1. Wind deformation

241 To break the radial symmetry inherent to our curve-based terrain
 242 generation and introduce more organic island shapes, we allow the
 243 user to define a wind velocity field via freehand strokes on a 2D
 244 canvas. Each stroke is represented as a parametric curve C , inter-
 245 preted as a local wind flow with direction C' , strength S , and influ-
 246 ence width σ . These strokes simulate wind and wave erosion effects
 247 on the terrain.

248 The deformation vector at any terrain point \mathbf{p} is computed as a
 249 sum over all strokes:

$$\Phi(\mathbf{p}) = \sum_{C \in \text{curves}} S \frac{C'(\mathbf{q})}{\|C'(\mathbf{q})\|} \cdot G_{\sigma}(\|\mathbf{p} - \mathbf{p}_C^*\|) \quad (2)$$

250 weighted by a Gaussian falloff centered on the closest point \mathbf{p}_C^*
 251 along each curve (Figure 7, top):

$$G_{\sigma}(x) = \frac{1}{\sigma\sqrt{2\pi}} e^{-\frac{x^2}{2\sigma^2}}. \quad (3)$$

252 To preserve semantic structure across terrain regions, a resis-
 253 tance function $\rho(\tilde{x})$ modulates the deformation based on terrain
 254 zones such as beach, lagoon, or abyss (Figure 8). The final defor-
 255 mation vector becomes:

$$\tilde{\Phi}(\mathbf{p}) = (1 - \rho(\tilde{x}_{\mathbf{p}})) \cdot \Phi(\mathbf{p}). \quad (4)$$

256 This warp is applied to both the height field and the label map,
 257 ensuring consistent semantic deformation. For example, applying
 258 strokes to one side of a circular island creates concave coastlines

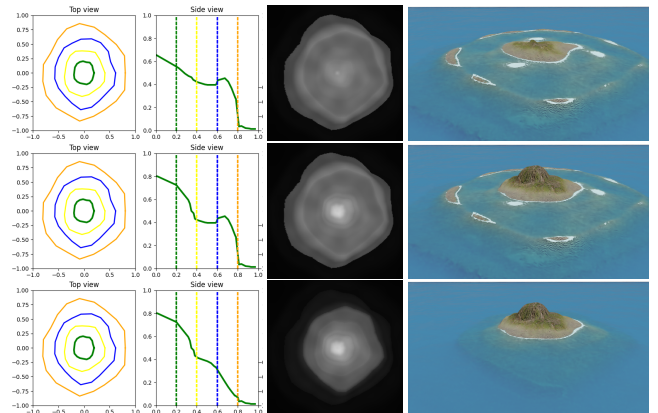


Figure 6: Providing a smooth function between each region results in islands with plausible reliefs. We fixed the outlines while editing only the height function in order to produce, from top to bottom, a low island, a coral reef island, and finally an identical island without the reef.

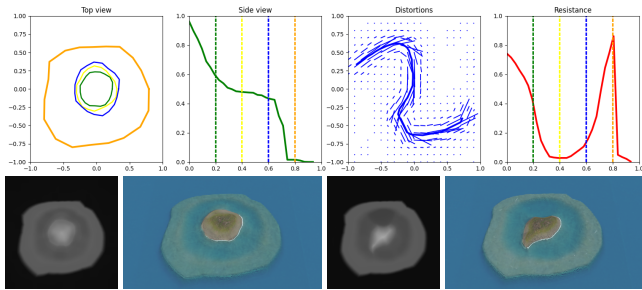


Figure 7: Defining a top-view wind vector field from user-provided strokes (top, blue) in association with a resistance function (top, red), a height field is deformed accordingly. Left: original height field and render; right: altered results. The beach and lagoon regions are defined with low resistance, which is visible by having only these regions deformed in bottom results.

259 while leaving high-resistance regions (e.g., the abyss) unaffected,
260 simulating the localized impact of natural erosion (Figure 7, bot-
261 tom).

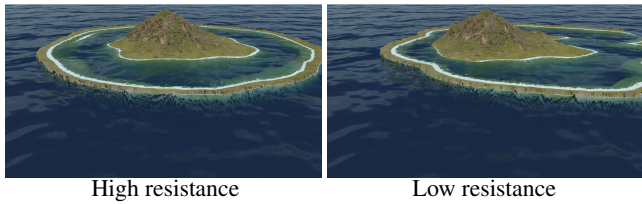


Figure 8: (Left) An island defined with a high resistance, under a uniform lateral wind velocity field, and (right) the same island with lower resistance on the reef borders, simulating the effect of coastal erosion.

4.2. Coral reef modeling

263 Once the terrain has been generated and deformed by the wind, we
264 simulate the long-term geological evolution of coral reef islands
265 through two parallel processes: the subsidence of the volcanic is-
266 land and the upward growth of coral reefs. As observed in nature,
267 the volcanic base sinks over time while coral formations grow ver-
268 tically to remain close to the water surface, following the "keep-up"
269 strategy of reef development.

4.2.1. Subsidence

271 Subsidence is modeled by uniformly scaling the original terrain
272 height downward, simulating the gradual sinking of the volcanic
273 landmass due to tectonic processes. The user specifies a subsidence
274 rate $\lambda \in [0, 1]$, which controls how much the island has sunk. The
275 subsided terrain is computed as:

$$h_{\text{subsid}}(\mathbf{p}) = (1 - \lambda) \cdot h_0(\mathbf{p}). \quad (5)$$

276 This factor is applied uniformly across the island, offering a geo-
277 logically plausible and computationally efficient approximation of
278 large-scale subsidence.

4.2.2. Coral reef growth

280 Coral reef growth is modeled independently from the subsiding ter-
281 rain. The system generates a coral-specific height field $h_{\text{coral}}(\mathbf{p})$
282 that remains near the sea surface regardless of the island's verti-
283 cal shift, reflecting coral growth in biologically viable depth ranges
284 (typically 0-30 meters below sea level).

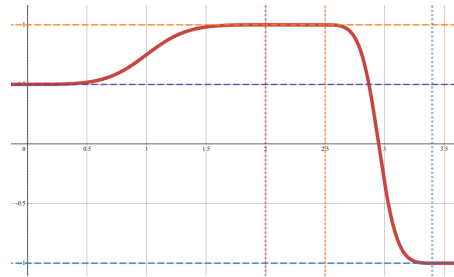


Figure 9: The modeling of the reef growth in our model is described by a piecewise function h_{coral} which is flat in the lagoon, the crest and abyss, and follows a smoothstep function as transitions for the backreef and fore reef regions. Zones' anchor heights are represented by horizontal dashed lines; zones' limits are dotted vertical lines.

We define distinct reef zones anchored at specific depths:

- Reef crest near sea level: $h_{\text{crest}} = -2 \text{ m}$,
- Back reef and lagoon: $h_{\text{back}} = -20 \text{ m}$,
- Fore reef sloping to abyss: $h_{\text{abyss}} = -100 \text{ m}$.

285 Each reef subregion is defined over a parametric domain $x \in$
286 $[0, 1]$, with $x = 0$ the beginning of the reef region and $x = 1$ its end,
287 directly inputting the parametric distance $x = \tilde{x} - i_{\text{reef region}}$. For in-
288 stance:

- Back reef: $x_{\text{back,start}} = 0, x_{\text{back,end}} = 0.5$,
- Reef crest: $x_{\text{crest,start}} = 0.75, x_{\text{crest,end}} = 0.8$,
- Abyss begins at $x_{\text{abyss,start}} = 1$.

296 We model transition zones between these regions using a
297 smoothstep operator:

$$\text{smoothstep}(x) = 3x^2 - 2x^3. \quad (6)$$

298 We denote the interpolating function as:

$$S(a, b, x_0, x_1, x) = a + (b - a) \text{smoothstep}\left(\frac{x - x_0}{x_1 - x_0}\right). \quad (7)$$

299 The complete coral height field, as displayed in Figure 9, is built

300 as a piecewise function:

$$h_{\text{coral}}(x) = \sum_{r \in \text{subregions}} \begin{cases} h_r & \text{if } x_{r,\text{start}} \leq x \leq x_{r,\text{end}} \\ 0 & \text{otherwise} \end{cases} + \sum_{t \in \text{transitions}} \begin{cases} S(h_t, h_{t+1}, x_{t,\text{end}}, x_{t+1,\text{start}}, x) & \text{if } x_{t,\text{end}} < x < x_{t+1,\text{start}} \\ 0 & \text{otherwise} \end{cases}$$
(8)

301 4.2.3. Output

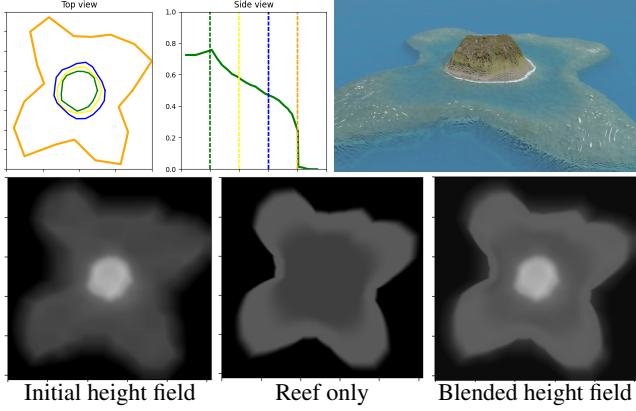


Figure 10: Volcano with single vent. (Bottom left) The initial height field is computed directly from the user input, (bottom center) the reef height field is outputed from Equation (8), and finally, (bottom right) we blend the two results with Equation (9).

302 Finally, we merge the island base height field and the coral reef
303 height field by our *ad-hoc* smooth maximum operator smax defined
304 as:

$$\text{smax}(a, b) = \begin{cases} a + \frac{\delta}{2k} \left(\frac{1}{1 + e^{-k\delta}} + \frac{1}{1 - e^{-k\delta}} \right) & \text{for } a \neq b \\ a + \frac{1}{2k} & \text{for } a = b \end{cases} \quad (9)$$

305 with $\delta = b - a$ for conciseness, and k a sharpness parameter approximating the max operator as k grows. At $k = 5$, the operator max is
306 already well approximated while conserving continuousness in the
307 resulting height field $\mathcal{H}(p) = \text{smax}(h_{\text{subsidi}}(\mathbf{p}), h_{\text{coral}}(\mathbf{p}))$.

308 The resulting terrain represents a plausible coral reef island,
309 where the volcanic island has subsided, and coral reefs have grown
310 upward to keep pace with the water level (Figure 10). The smooth
311 blending between the subsided terrain and the coral features ensures
312 a natural transition between regions like the island, lagoon,
313 and coral reefs.

315 5. Data generation

316 The creation of the dataset is done through the use of the procedural
317 curve-based modeling algorithm for which we alter the input
318 parameters. For each generation, the top-view and profile-view
319 sketches use an initial layout. Each outline of the top-view sketch
320 is defined as a centered circle of random radius $r_{\min} \leq r^* \leq r_{\max}$.

321 We add another deformation based on fBm noise η such that the
322 final contour, profile, and resistances, are defined as

$$\begin{aligned} r(\theta) &= r^* + \eta_{\text{contours}}(\theta) \\ h_{\text{profile}}(\tilde{x}) &= h_{\text{profile}}^*(\tilde{x}) \cdot \eta_{\text{profile}}(\tilde{x}) \\ \rho(\tilde{x}) &= \rho^*(\tilde{x}) \cdot \eta_{\text{resistance}}(\tilde{x}) \end{aligned}$$

323 Finally, a wind velocity field is randomly generated as a final input
324 for the curve-based modeling algorithm, introducing deformations
325 on the resulting islands. The realistic nature of wind is ignored
326 for the generation of the wind strokes in order to provide complexity
327 and variety in the results. We generate a random number n of
328 strokes and their path by a uniformly sampling a random number m
329 of points. The spread and intensity of each stroke is also random.

330 Once all inputs are set, we generate an example for multiple level
331 of subsidence $\lambda \in [0, 1]$ to obtain a height field incorporating the
332 coral reef modeling and the associated label map.

333 We use of the Hue component to encode the labels directly from
334 the parametric distance $H = |\tilde{x}|$ while the subsidence rate into the
335 Value component $V = \lambda$. Moreover, we purposefully left the Saturation
336 component unchanged at this stage, reserving space for potentially
337 including another parameter in the future.

338 Data augmentation

339 To enhance the variety of the dataset and improve the model's
340 ability to generalize, we apply several data augmentation techniques
341 in addition of the usual affine transformations (rotation, scaling,
342 and flipping):

343 *Translation:* Since the original algorithm always centers the island,
344 we translate the islands within the image to remove this constraint
345 (Figure 11, leftmost). This ensures that the cGAN can generate
346 islands in any position within the frame. By wrapping the island
347 on the borders, the model learns that data can appear on the edges
348 on the image.

349 *Copy-paste:* In some cases, we combine multiple islands into a
350 single sample, with only a maximum intersection over union (IoU)
351 of 10%, allowing the abysses to overlap but without obtaining other
352 region types to merge. Height fields blending is done through the
353 smooth maximum function from Equation (9), and the label blending
354 uses the usual max operator. The regions not covered by any
355 island are assigned the abyss ID, which is very close to the minimal
356 height, meaning that in this case specifically, the subsidence
357 factor (Value channel) is close to irrelevant (Figure 11, rightmost).

358 All augmentation techniques are applied both to the height field

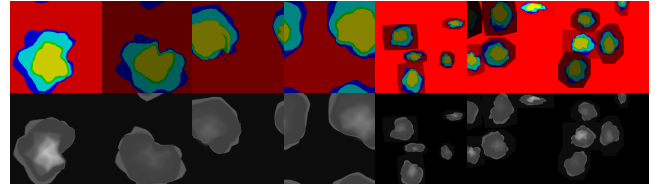


Figure 11: Examples from a dataset with increasing data augmentation.

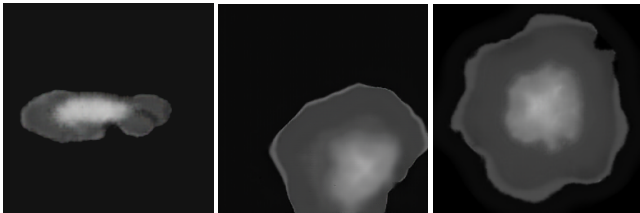


Figure 12: After the first epoch (left), grid artifacts similar to low resolution image are visible, but are being corrected during a second epoch (middle) where erosion patterns appear in the height fields (right).

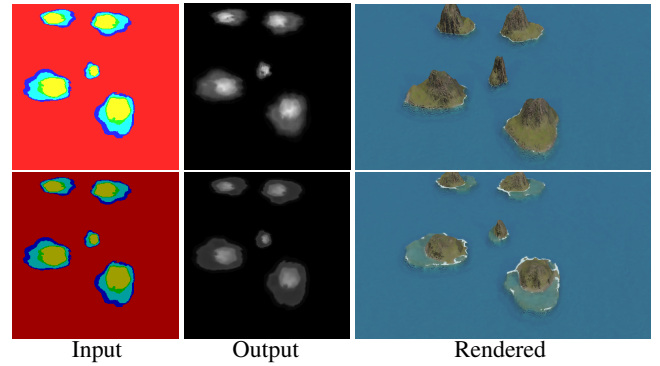


Figure 13: An identical label map yield similar height fields over multiple inferences from the model, even after modifying the subsidence factor (visible in the luminosity of the input image).

and the label map simultaneously to ensure consistency between the input (the label map) and the output (the height field).

6. Learning-based generation

In this section, we introduce the use of a conditional Generative Adversarial Network (cGAN), specifically the pix2pix model proposed by Isola et al., 2017, to enhance the island generation process by increasing the variety and flexibility of terrains. While the curve-based modeling algorithm can create numerous island examples, cGAN provides additional flexibility in generating more complex terrain without the rigid constraints of the curve-based algorithm that stem from our initial assumptions based on coral reef formation theory.

The training was performed using a batch size of 1, and optimized using the Adam optimizer with a learning rate of 0.0002 and momentum parameters $\beta_1 = 0.5$ and $\beta_2 = 0.999$. The loss function combined a conditional adversarial loss and an L1 loss, where the L1 loss was weighted by a factor $\lambda = 100$. The generator follows a U-Net architecture with encoder-decoder layers and skip connections, while the discriminator was based on a PatchGAN, classifying local image patches. These parameters are directly used from the original paper.

The inference of our model, with a dataset of approximatively 10 000 examples representing about 30 minutes of training, still outputs grid artifacts, visible in Figure 12. After the second epoch, visual artifacts are already rare. This training time seems long but, at the best of our knowledge, is the shortest training time for terrain generation with learning-based approach in the litterature, mostly due to the synthetic nature of our dataset.

Once the model is trained, the user colors a 256×256 RGB image to sketch the different regions. Each region is given a specific color based on the HSV encoding used for the dataset generation. The examples presented in this paper uses red for abysses, blue for reefs, cyan for lagoons, green for beaches and yellow for mountains. The subsidence factor presented in Section 4.2.1 is controllable through the luminosity of the input image.

The Python script for the initial island dataset generation is poorly optimized and takes about 2.5s per island of size 256×256 as we do not perform parallelization here. Implementing an opti-

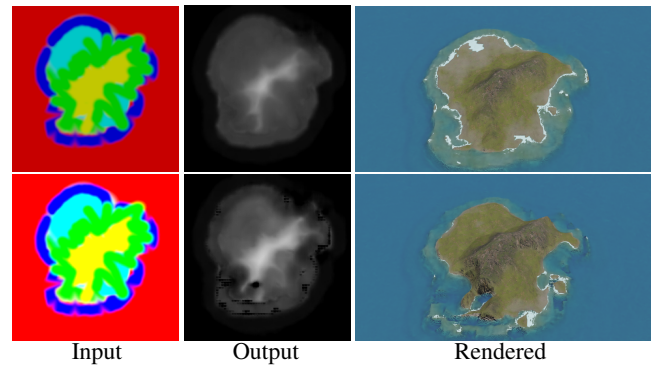


Figure 14: User applied fuzzy brushes to draw the label map, resulting in some pixels that are inconsistent with the dataset and unlogical island layouts: abyss regions (red) are found between beach (green), lagoon (cyan) and reef regions (blue). The neural model ignores the layout inconsistencies, and partially over-brightness as long as the pixel isn't completely white.

mized C++ version of the initial generation process reduces this execution time to 50ms per generation.

On the other hand, the inference time of our deep learning model for a single input image of dimension 256×256 is constant whatever the complexity of the scene. Using the NVIDIA GeForce GTX 1650 Ti GPU with Python 3.10 and PyTorch version 2.5.1+cu121, the inference time measured is 5ms (std 1.1ms).

7. Results

The resulting model for coral island generation enables a high control-level from a user perspective as the unconstraint painting allows for complex scenarios while producing in real-time the resulting height fields. In this paper we used the software Blender to provide renders directly from the outputted height fields. As our pix2pix model is trained to output 256×256 images, the resolution of the 3D models is limited by this architecture.

Using deep-learning-based models, most constraints from our initial assumptions are lifted (radial layout, isolated islands, ...).

414 The control over the overall shapes of the islands regions are given
 415 through digital painting, here using the GIMP software. Each pixel
 416 of the image are encoded in HSV, with the region identifier encoded
 417 in the Hue channel. The user may increase or decrease the subsi-
 418 dence level of the island by modifying the Value channel over the
 419 whole image (see Figure 13).

420 Since the model is based on statistics over the pixel values in-
 421 stead of hard values, users are not limited to a finite number of
 422 region identifiers, meaning that the output is more or less robust to
 423 noise (due to image compression, for example) and to the fuzzy val-
 424 ues resulting from anti-aliasing of brushes often set by default, or
 425 resizing algorithm, by image editors, or even due to compression
 426 algorithm. The example displayed in Figure 14 presents a sketch
 427 for which the outlines of the regions are at the same time blurry and
 428 with layouts that are not expected (such as the small red re-
 429 gions inside the southern lagoon region or the adjacency of beach
 430 regions directly with the abyssal region) on the top figure and show-
 431 ing highlight clipping on the bottom figure. The learned model does
 432 not include inconsistancies and results in plausible 3D models. We
 433 can note that the input label map doesn't require to be hand drawn,
 434 as a simple Perlin noise can produce it randomly, as shown in the
 435 examples of Figure 17.

436 The tolerance over the input values may be used to provide even
 437 more control about the transitions between two regions. Figure 15
 438 shows an example of input map with regions that are leaking over
 439 neighboring regions, and the introduction of new hue values non-
 440 existant in the dataset (light green and dark green) but are the inter-
 441 polated hue value of mountain regions and beach regions.

442 Since the curve-based procedural phase included low random-
 443 ness, the output of the cGAN is limiting its unpredictability and the
 444 results to a slight change on the input create only slight changes on
 445 the output, preventing unexpected results. Figure 13 shows the re-
 446 sult of an input map with only a variation on the subsidence level,
 447 the resulting height fields are very similar. Adding the real-time
 448 computation of outputs, it becomes possible to construct progres-
 449 sively a landscape and correct small mistakes to intuitively design
 450 islands inspired by real-world regions. A creation of an island simi-
 451 lar to Mayotte, presented in Figure 16 was hand-made in few min-
 452 utes.

453 **Limitations** While this approach brings significant advantages,
 454 there are also some limitations to consider. The reliance on a syn-
 455 thetic dataset means that the cGAN inherits some biases and lim-

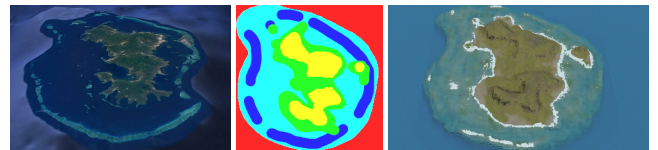


Figure 16: Comparison between real (left, from Google Earth) and synthetic (right) islands of Mayotte. The label map (center) is hand drawn to match approximatively its real-world counterpart.

456 iterations of our or initial curve-based algorithm. This could limit
 457 the true diversity of the terrains that the model can generate, as the
 458 output is confined by the patterns present in the training data. Addi-
 459 tionally, the cGAN model's internal logic lacks transparency, offer-
 460 ing limited user control over the generation process once the model
 461 has been trained. Moreover the training time is far from real-time.

462 **Future work** Further improvements could be made to the synthetic
 463 dataset. Incorporating more complex geological processes, such as
 464 wave erosion or tidal influences, could lead to even more realistic
 465 terrains. Additionally, refining the way islands are blended in multi-
 466 island samples, or adding more diverse input conditions (e.g., dif-
 467 ferent geological settings), could help the model generalize better
 468 and produce more varied and dynamic landscapes. While the cur-
 469 rent model allows for rapid terrain generation, adding more options
 470 for users to interact with the cGAN, such as tweaking parameters
 471 like wind strength or island size, could enhance the flexibility of the
 472 system. Many other neural networks models could be exploited to
 473 increase the possibilities, such as newer variants of cGANs (Park
 474 et al., 2019), or models with style transfer functionalities (Gatys
 475 et al., 2015; Zhu et al., 2020) in order to change the overall aspect
 476 of a terrain (Perche et al., 2023b, 2023a), use text-to-images mod-
 477 els (Rombach et al., 2021; Radford et al., 2021) to generate height
 478 fields from a verbal prompt, or super-resolution models (Dong et
 479 al., 2014) to increase the definition of details in the final output
 480 (Guérin, Digne, Galin, and Peytavie, 2016).

8. Conclusion and future work

482 This work has presented a novel approach to generating coral reef
 483 island terrains by combining traditional procedural methods with
 484 deep learning techniques. We first developed a procedural genera-
 485 tion algorithm capable of creating a wide variety of island terrains
 486 through a combination of top-view and profile-view sketches, wind
 487 deformation, and subsidence and coral reef growth simulation. By
 488 applying these methods, we were able to produce realistic terrains
 489 based on geological processes, capturing key features of coral reef
 490 islands such as beaches, lagoons, and coral reefs.

491 To further enhance flexibility and realism in the generation pro-
 492 cess, we incorporated a conditional Generative Adversarial Net-
 493 work (cGAN), using the pix2pix model to generate height maps
 494 from label maps of island features. The cGAN model allowed us to
 495 overcome some of the constraints inherent in the procedural algo-
 496 rithm, such as radial symmetry and fixed island positioning. With
 497 data augmentation techniques, we were able to train the cGAN on
 498 a synthetic dataset, generating varied and realistic island terrains.

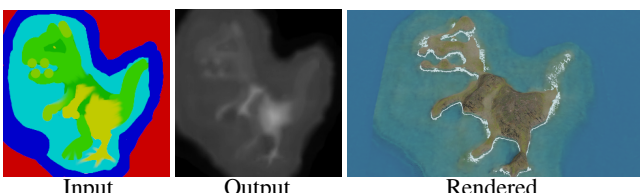


Figure 15: Without constraints on the generation, the user may use unrealistic layout and the neural network will however output a plausible result. Here new colors have been added (pistachio), but the network naturally considers it as a transition from mountain to beach.

- 499 **References**
- 500 Beckham, C., & Pal, C. (2017). A step towards procedural terrain
501 generation with gans. <http://arxiv.org/abs/1707.03383>
502 (cit. on p. 2).
- 503 Beneš, B., Těšínský, V., Hornyš, J., & Bhatia, S. K. (2006). Hy-
504 draulic erosion. *Computer Animation and Virtual Worlds*,
505 17, 99–108. <https://doi.org/10.1002/cav.77> (cit. on p. 2).
- 506 Cordonnier, G., Braun, J., Cani, M.-P., Benes, B., Galin, É., Pey-
507 tavie, A., & Guérin, É. (2016). Large scale terrain gener-
508 ation from tectonic uplift and fluvial erosion. *Computer*
509 *Graphics Forum*, 35, 165–175. <https://doi.org/10.1111/cgf.12820> (cit. on p. 2).
- 510 Cordonnier, G., Cani, M.-P., Beneš, B., Braun, J., & Galin, É.
511 (2017). Sculpting mountains: Interactive terrain model-
512 ing based on subsurface geology. *IEEE Transactions on*
513 *Visualization and Computer Graphics*, 24. <https://doi.org/10.1109/TVCG.2017.2689022> (cit. on p. 2).
- 514 Cordonnier, G., Galin, É., Gain, J., Beneš, B., Guérin, É., Peytavie,
515 A., & Cani, M.-P. (2017). Authoring landscapes by com-
516 bining ecosystem and terrain erosion simulation. *ACM*
517 *Transactions on Graphics*, 36. <https://doi.org/10.1145/3072959.3073667> (cit. on p. 2).
- 518 Dong, C., Loy, C. C., He, K., & Tang, X. (2014). Image super-
519 resolution using deep convolutional networks. <http://arxiv.org/abs/1501.00092> (cit. on p. 8).
- 520 Ebert, D. S., Peachey, D., Worley, S., Hart, J. C., Musgrave, K.,
521 Perlin, K., & Mark, W. R. (2003). *Texturing and model-
522 ing, a procedural approach* (Vol. Third edition). Morgan
523 Kaufmann. (Cit. on p. 2).
- 524 Ecormier-Nocca, P., Cordonnier, G., Carrez, P., Moigne, A. M.,
525 Memari, P., Benes, B., & Cani, M. P. (2021). Authoring
526 consistent landscapes with flora and fauna. *ACM Trans-
527 actions on Graphics*, 40. <https://doi.org/10.1145/3450626.3459952> (cit. on p. 2).
- 528 Fournier, A., Fussell, D., & Carpenter, L. (1982). Computer ren-
529 dering of stochastic models. *Communications of the ACM*,
530 25, 371–384. <https://doi.org/10.1145/358523.358553>
531 (cit. on p. 2).
- 532 Gain, J., Marais, P., & Straßer, W. (2009). Terrain sketching. *Pro-
533 ceedings of I3D 2009: The 2009 ACM SIGGRAPH Sym-
534 posium on Interactive 3D Graphics and Games*, 1, 31–
535 38. <https://doi.org/10.1145/1507149.1507155> (cit. on
536 p. 2).
- 537 Galin, E., Guérin, E., Peytavie, A., Cordonnier, G., Cani, M.-P.,
538 Benes, B., & Gain, J. (2019). A review of digital ter-
539 rain modeling. *Computer Graphics Forum*, 38, 553–577.
540 <https://doi.org/10.1111/cgf.13657> (cit. on p. 2).
- 541 Gasch, C., Chover, M., Remolar, I., & Rebollo, C. (2020). Pro-
542 cedural modelling of terrains with constraints. *Multimedia*
543 *Tools and Applications*, 79, 31125–31146. <https://doi.org/10.1007/s11042-020-09476-3> (cit. on p. 2).
- 544 Gatys, L. A., Ecker, A. S., & Bethge, M. (2015). A neural algorithm
545 of artistic style. <http://arxiv.org/abs/1508.06576> (cit. on
546 p. 8).
- 547 Génevaux, J.-D., Galin, É., Peytavie, A., Guérin, É., Briquet, C.,
548 Grosbellet, F., & Beneš, B. (2015). Terrain modelling
549 from feature primitives. <https://doi.org/https://doi.org/10.1111/cgf.12530> (cit. on p. 2).
- 550 Guérin, E., Peytavie, A., Masnou, S., Digne, J., Sauvage, B., Gain,
551 J., & Galin, E. (2022). Gradient terrain authoring. *Com-
552 puter Graphics Forum*, 41, 85–95. <https://doi.org/10.1111/cgf.14460> (cit. on p. 2).
- 553 Guérin, É., Digne, J., Galin, É., & Peytavie, A. (2016). Sparse
554 representation of terrains for procedural modeling. *Com-
555 puter Graphics Forum*, 35, 177–187. <https://doi.org/10.1111/cgf.12821> (cit. on p. 8).
- 556 Guérin, É., Digne, J., Galin, É., Peytavie, A., Wolf, C., Beneš,
557 B., & Martinez, B. (2017). Interactive example-based
558 terrain authoring with conditional generative adversar-
559 ial networks. *ACM Transactions on Graphics*, 36. <https://doi.org/10.1145/3130800.3130804> (cit. on p. 2).
- 560 Hnaidi, H., Guérin, E., Akkouche, S., Peytavie, A., & Galin, E.
561 (2010). Feature based terrain generation using diffusion
562 equation. *Computer Graphics Forum*, 29, 2179–2186.
563 <https://doi.org/10.1111/j.1467-8659.2010.01806.x>
564 (cit. on p. 2).
- 565 Hopley, D. (2014). *Encyclopedia of modern coral reefs : Structure,
566 form and process*. Springer, Credo Reference. (Cit. on
567 p. 1).
- 568 Isola, P., Zhu, J.-Y., Zhou, T., & Efros, A. A. (2017). Image-to-
569 image translation with conditional adversarial networks.
570 *2017 IEEE Conference on Computer Vision and Pattern*
571 *Recognition (CVPR)*, 5967–5976. <https://doi.org/10.1109/CVPR.2017.632> (cit. on pp. 2, 7).
- 572 Körner, C., Spehn, E. M., Bugmann, H., & Zurich, E. (2014).
573 *Mountain systems* (tech. rep.). <https://www.researchgate.net/publication/238663492> (cit. on p. 1).
- 574 Lyons, M. B., Murray, N. J., Kennedy, E. V., Kovacs, E. M.,
575 Castro-Sanguino, C., Phinn, S. R., Acevedo, R. B., Al-
576 varez, A. O., Say, C., Tudman, P., Markey, K., Roe, M.,
577 Canto, R. F., Fox, H. E., Bambic, B., Lieb, Z., Asner,
578 G. P., Martin, P. M., Knapp, D. E., ... Roelfsema, C. M.
579 (2024). New global area estimates for coral reefs from
580 high-resolution mapping. *Cell Reports Sustainability*, 1,
581 100015. <https://doi.org/10.1016/j.crsus.2024.100015>
582 (cit. on p. 1).
- 583 Mei, X., Decaudin, P., & Hu, B. G. (2007). Fast hydraulic ero-
584 sion simulation and visualization on gpu. *Proceedings -
585 Pacific Conference on Computer Graphics and Applica-
586 tions*, 47–56. <https://doi.org/10.1109/PG.2007.27> (cit. on
587 p. 2).
- 588 Mirza, M., & Osindero, S. (2014). Conditional generative adversar-
589 ial nets. <http://arxiv.org/abs/1411.1784> (cit. on p. 2).
- 590 Musgrave, F. K., Kolb, C. E., & Mace, R. S. (1989). The synthesis
591 and rendering of eroded fractal terrains. *Proceedings of*
592 *the 16th Annual Conference on Computer Graphics and*
593 *Interactive Techniques, SIGGRAPH 1989*, 41–50. <https://doi.org/10.1145/74333.74337> (cit. on p. 2).
- 594 Natali, M., Viola, I., & Patel, D. (2012). Rapid visualization of
595 geological concepts. *Brazilian Symposium of Computer*
596 *Graphic and Image Processing*, 150–157. <https://doi.org/10.1109/SIBGRAPI.2012.29> (cit. on p. 2).
- 597 Neidhold, B., Wacker, M., & Deussen, O. (2005). Interactive phys-
598 ically based fluid and erosion simulation. *Natural Phe-*
599 *nomena*, 1, 1–10.
- 600

- 613 *nomena*, 25–32. <http://graphics.uni-konstanz.de/~publikationen/Neidhold2005InteractivePhysicallyBased/Neidhold2005InteractivePhysicallyBased.pdf> (cit. on p. 2).
- 614 Olsen, J. (2004). Realtime procedural terrain generation. *Department of Mathematics And Computer Science*, 20. <https://pdfs.semanticscholar.org/5961/c577478f21707dad53905362e0ec4e6ec644.pdf> (%5Cnhttp://www.tsi.enst.fr/~bloch/P6/PRREC/terrain_generation.pdf%5Cnhttp://web.mit.edu/cesium/Public/terrain.pdf) (cit. on p. 2).
- 615 Panagiotou, E., & Charou, E. (2020). Procedural 3d terrain generation using generative adversarial networks. <http://arxiv.org/abs/2010.06411> (cit. on p. 2).
- 616 Park, J., Redwine, J., Hill, T. D., & Kotun, K. (2019). Water resource and ecotone transformation in coastal ecosystems. *Ecological Modelling*, 405, 69–85. <https://doi.org/10.1016/j.ecolmodel.2019.04.015> (cit. on p. 8).
- 617 Perche, S., Peytavie, A., Benes, B., Galin, E., & Guérin, E. (2023a). Styledem: A versatile model for authoring terrains. <http://arxiv.org/abs/2304.09626> (cit. on p. 8).
- 618 Perche, S., Peytavie, A., Benes, B., Galin, E., & Guérin, E. (2023b). Authoring terrains with spatialised style. *Computer Graphics Forum*, 42. <https://doi.org/10.1111/cgf.14936> (cit. on p. 8).
- 619 Perlin, K. (1985). An image synthesizer. *ACM SIGGRAPH Computer Graphics*, 19, 287–296. <https://doi.org/10.1145/325165.325247> (cit. on p. 2).
- 620 Perlin, K. (2001). Noise hardware. *Real-Time Shading SIGGRAPH Course Notes* (cit. on p. 2).
- 621 Radford, A., Kim, J. W., Hallacy, C., Ramesh, A., Goh, G., Agarwal, S., Sastry, G., Askell, A., Mishkin, P., Clark, J., Krueger, G., & Sutskever, I. (2021). Learning transferable visual models from natural language supervision. <http://arxiv.org/abs/2103.00020> (cit. on p. 8).
- 622 Rombach, R., Blattmann, A., Lorenz, D., Esser, P., & Ommer, B. (2021). High-resolution image synthesis with latent diffusion models. <http://arxiv.org/abs/2112.10752> (cit. on p. 8).
- 623 Schott, H., Paris, A., Fournier, L., Guérin, E., & Galin, E. (2023). Large-scale terrain authoring through interactive erosion simulation. *ACM Transactions on Graphics*, 42, 1–15. <https://doi.org/10.1145/3592787> (cit. on p. 2).
- 624 Sisodia, Y. (2022). Gan-generated terrain for game assets. *Indian Journal of Artificial Intelligence and Neural Networking*, 2, 1–3. <https://doi.org/10.54105/ijainn.F1060.102622> (cit. on p. 2).
- 625 Smelik, R. M., Kraker, K. J. D., Groenewegen, S. A., Tutenel, T., & Bidarra, R. (2009). A survey of procedural methods for terrain modelling. *Proceedings of the CASA workshop on 3D advanced media in gaming and simulation (3AMIGAS)* (cit. on p. 2).
- 626 Spick, R., & Walker, J. A. (2019). Realistic and textured terrain generation using gans. *Proceedings - CVMP 2019: 16th ACM SIGGRAPH European Conference on Visual Media Production*. <https://doi.org/10.1145/3359998.3369407> (cit. on p. 2).
- 627 Talgorn, F. X., & Belhadj, F. (2018). Real-time sketch-based terrain generation. *ACM International Conference Proceeding Series*, 13–18. <https://doi.org/10.1145/3208159.3208184> (cit. on p. 2).
- 628 Voulgaris, G., Mademlis, I., & Pitas, I. (2021). Procedural terrain generation using generative adversarial networks. *European Signal Processing Conference, 2021-August*, 686–690. <https://doi.org/10.23919/EUSIPCO54536.2021.9616151> (cit. on p. 2).
- 629 Wulff-Jensen, A., Rant, N. N., Møller, T. N., & Billeskov, J. A. (2018, January). Deep convolutional generative adversarial network for procedural 3d landscape generation based on dem. In *Interactivity, game creation, design, learning, and innovation* (pp. 85–94). Springer. https://doi.org/10.1007/978-3-319-76908-0_9 (cit. on p. 2).
- 630 Zhu, D., Cheng, X., Zhang, F., Yao, X., Gao, Y., & Liu, Y. (2020). Spatial interpolation using conditional generative adversarial neural networks. *International Journal of Geographical Information Science*, 34, 735–758. <https://doi.org/10.1080/13658816.2019.1599122> (cit. on p. 8).

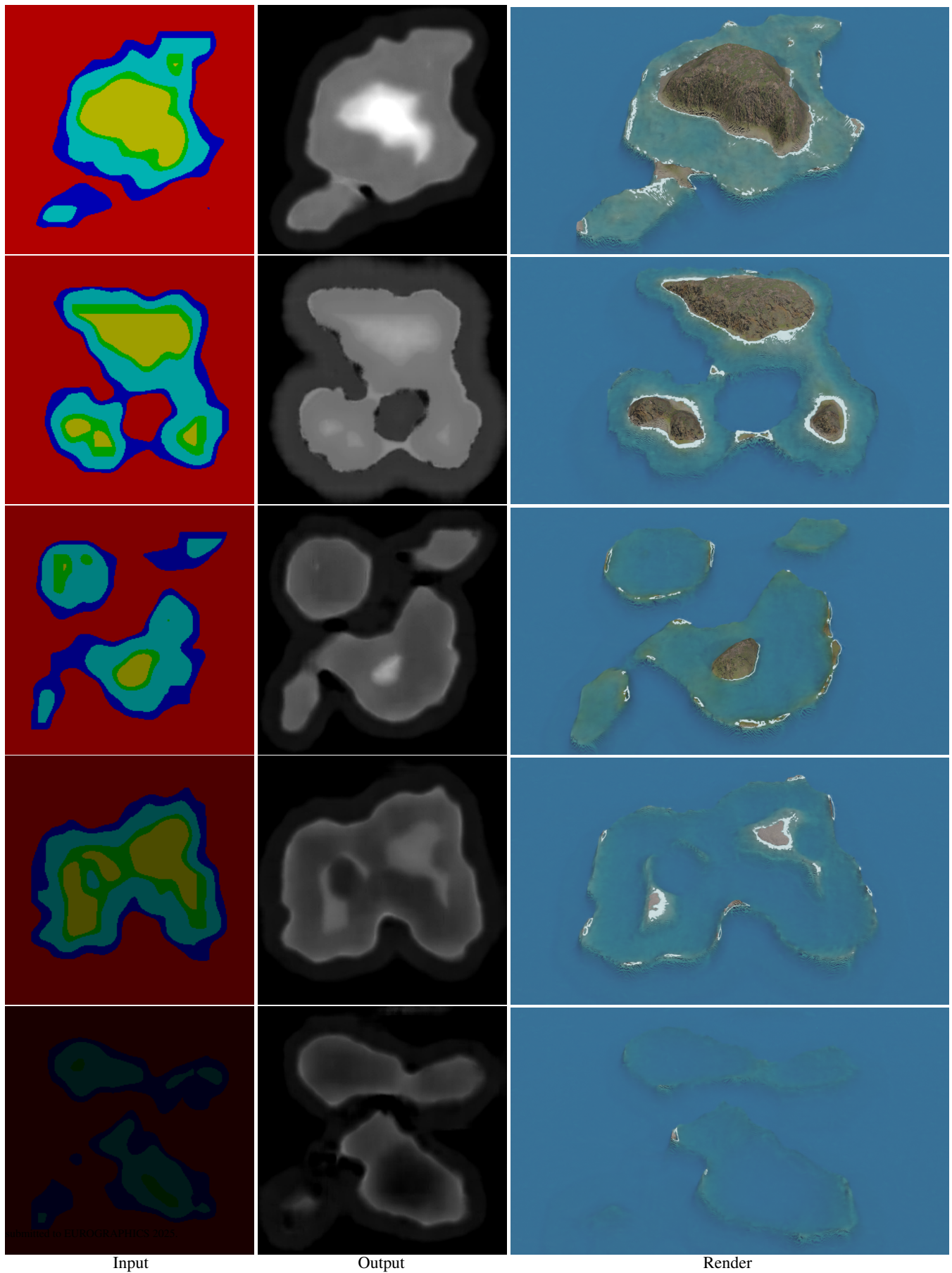


Figure 17: Starting from random Perlin noise, transformed into label maps with increasing subsidence, we can generate a large variety of results.

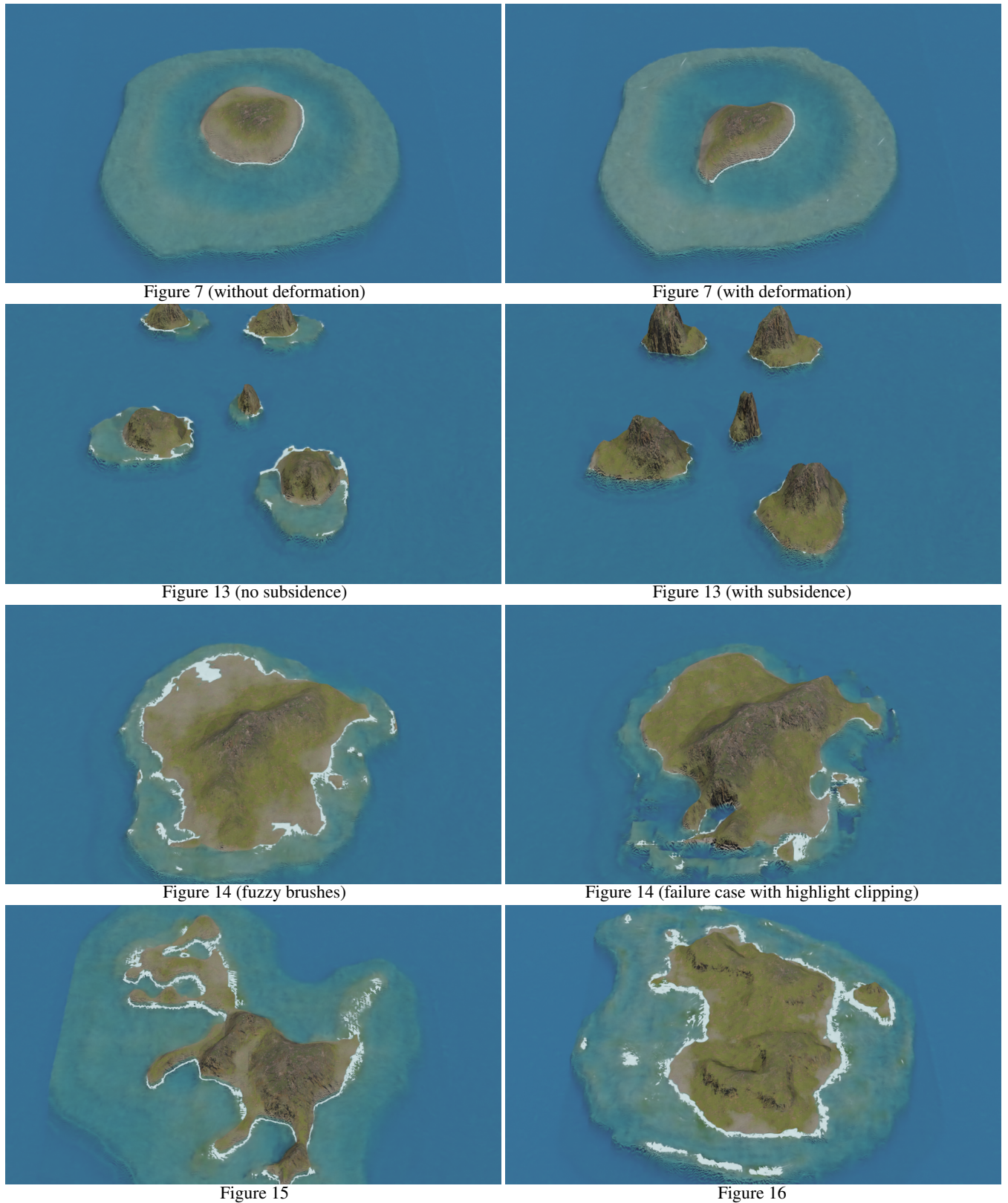


Figure 18: High-resolution version of figures found in this paper.